Applied Energy 126 (2014) 182–189

Contents lists available at ScienceDirect

Applied Energy

journal homepage: www.elsevier.com/locate/apenergy

Method for estimating capacity and predicting remaining useful life of lithium-ion battery

Chao Hu *, Gaurav Jain, Prabhakar Tamirisa, Tom Gorka

Medtronic Energy and Component Center, Brooklyn Center, MN 55430, USA

HIGHLIGHTS

- We develop an integrated method for the capacity estimation and RUL prediction.
- A state projection scheme is derived for capacity estimation.
- The Gauss–Hermite particle filter technique is used for the RUL prediction.
- Results with 10 years' continuous cycling data verify the effectiveness of the method.

ARTICLE INFO

Article history:
Received 1 November 2013
Received in revised form 18 February 2014
Accepted 31 March 2014
Available online 8 May 2014

Keywords:
Capacity
Health monitoring
Prognostics
Remaining useful life
Lithium-ion battery

ABSTRACT

Reliability of lithium-ion (Li-ion) rechargeable batteries used in implantable medical devices has been recognized as of high importance from a broad range of stakeholders, including medical device manufacturers, regulatory agencies, physicians, and patients. To ensure Li-ion batteries in these devices operate reliably, it is important to be able to assess the capacity of Li-ion battery and predict the remaining useful life (RUL) throughout the whole life-time. This paper presents an integrated method for the capacity estimation and RUL prediction of Li-ion battery used in implantable medical devices. A state projection scheme from the author's previous study is used for the capacity estimation. Then, based on the capacity estimates, the Gauss–Hermite particle filter technique is used to project the capacity fade to the end-of-service (EOS) value (or the failure limit) for the RUL prediction. Results of 10 years' continuous cycling test on Li-ion prismatic cells in the lab suggest that the proposed method achieves good accuracy in the capacity estimation and captures the uncertainty in the RUL prediction. Post-explant weekly cycling data obtained from field cells with 4–7 implant years further verify the effectiveness of the proposed method in the capacity estimation.

1. Introduction

As a Li-ion battery cell ages, the cell capacity directly limits the electrical performance through energy loss [1]. Capacity, which quantifies the available energy stored in a fully charged Li-ion battery cell, is an important indicator of the health condition of the battery cell; remaining useful life, also called remaining longevity, refers to the available service time left before the capacity fade reaches an unacceptable level. It is important to accurately estimate these parameters in order to monitor the present battery SOH and to enable failure prevention through effective maintenance actions.

Recent literature reports various approaches to estimate the SOH with a focus on the capacity estimation. Joint/dual extended Kalman filter (EKF) [1] and unscented Kalman filter [2] with an enhanced self-correcting model were proposed to simultaneously estimate the state of charge (SOC), capacity and resistance. To improve the performance of joint/dual estimation, adaptive measurement noise models of the Kalman filter were recently developed to separate the sequence of SOC and capacity estimation [3]. A physics-based single particle model was used to simulate the life cycling data of Li-ion battery and to study the physics of capacity fade [4,5]. New techniques for SOH estimation were developed based on a coulomb counting technique with dynamic re-calibration of the cell capacity [6] and the approximate entropies of cell terminal voltage and current [7]. A multiscale computational scheme was developed that decouples the SOC and capacity estimation with respect to both the measurement- and time-scales and employs a state projection schedule for accurate and stable capacity estimation [8]. A newly developed online fitting approach estimates the electromotive force through fitting a reference open

* Corresponding author. Tel.: +1 763 514 0231; fax: +1 763 514 1284.
E-mail address: chao.x.hu@medtronic.com (C. Hu).

http://dx.doi.org/10.1016/j.apenergy.2014.03.086
0306-2619/

circuit voltage (OCV) relaxation model to the measured OCV relaxation curve, which was applied to estimating the SOC and capacity of the Li-ion battery in an electrical vehicle [9]. Most recently, a data-driven multi-scale EKF algorithm was developed that leverages the fast-varying characteristic of SOC and the slow-varying characteristic of capacity, with an aim to achieve accurate SOC and capacity estimation in real-time [10].

Research on RUL prediction of Li-ion battery was mainly conducted by researchers in the prognostics and health management (PHM) society. A Bayesian framework combining the relevance vector machine (RVM) and particle filter was proposed for prognostics (i.e., RUL prediction) of Li-ion battery based on impedance measurement [11]. In order to eliminate the reliance of prognostics on impedance measurement equipment, researchers developed an empirical circuit model to model the electrical characteristics of a battery cell and employed the particle filter to predict the RULs for individual discharge cycles as well as for the whole life-time [12]. An adaptive recurrent neural network was proposed for system dynamic state forecasting with an aim to predict the RUL of Li-ion battery [13]. Most recently, a naive Bayes model was developed for RUL prediction of Li-ion battery under constant operating conditions at multiple ambient temperatures and discharge currents [14].

Despite significant advances in the capacity estimation and RUL prediction of Li-ion batteries, research innovations are still needed to develop new, simple and integrated methods. In this paper, an integrated method for estimating the capacity and predicting the RUL is proposed and applied to a Li-ion battery used in implantable medical devices. A state projection scheme from the author's previous study [8] is used for the capacity estimation. Then, based on the capacity estimates, the Gauss–Hermite particle filter (GHPF) technique is used to track the capacity fade trend and extrapolate the future capacity values for the RUL prediction. 10 years' continuous cycling data on four test cells in the lab as well as post-explant cycling data of four field cells with 4–7 implant years are used to demonstrate the effectiveness of the proposed method. This paper is organized as follows. Section 2 presents the fundamentals of the proposed method. The method is applied to a Li-ion battery used in implantable medical devices. Section 3 discusses the experimental results of this application. The paper is concluded in Section 4.

2. Technical approach

In a Li-ion battery cell, the SOC quantifies the remaining charge of a cell relative to the full capacity. The SOC of a cell changes very rapidly and, depending on the use condition, may traverse the entire range 100–0% within minutes. In contrast to the rapidly varying behavior of the SOC, the cell capacity tends to vary very slowly and typically decreases 1.0% or less in a month with regular use. Given a discrete-time dynamic model that describes the electrical behavior of a cell and knowledge of the measured electrical signals, we are interested in estimating the capacity of the cell in a dynamic environment at every charge/discharge cycle and predict how long the cell is expected to last before the capacity fade reaches an unacceptable level. The subsequent sections are dedicated to describing our proposed approach for doing so. Section 2.1 presents the discrete-time cell dynamic model; Section 2.2 describes the state projection scheme for the capacity estimation; and Section 2.3 presents the Gauss–Hermite particle filter for the RUL prediction.

2.1. Discrete-time cell dynamic model

The SOC estimation is essential to the capacity estimation. In order to estimate the SOC in a dynamic environment, we need a cell dynamic model that relates the SOC to the cell terminal voltage. Here we can use a simplified equivalent circuit model (or lumped parameter model), as shown in Fig. 1, which considers the effects of OCV, series resistance (R_s), diffusion resistance (R_d), and diffusion capacitance (C_d) [3]. The model expresses the cell terminal voltage as

$$V_k = \mathrm{OCV}(\mathrm{SOC}_k) - i_k \cdot R_s - V_{d,k} \tag{1}$$

where OCV is the open circuit voltage, i the current, R_s series resistance, V_d the diffusion voltage, and k the index of the measurement time step. Since there is a strong correlation between the SOC and OCV, the SOC can be estimated from the OCV of the cell. The state transition equation of the diffusion voltage can be expressed as

$$V_{d,k+1} = V_{d,k} + \left(i_k - \frac{V_{d,k}}{R_d}\right) \cdot \frac{\Delta t}{C_d} \tag{2}$$

where R_d is the diffusion resistance, C_d the diffusion capacitance, and Δt the length of measurement interval. The time constant of the diffusion system can be expressed as $\tau = R_d C_d$. It is noted that, after a sufficiently long duration (e.g., 5τ) with a constant current i_k, the system reaches the final steady state with a final voltage $V_d = i_k \cdot R_d$ and the cell terminal voltage becomes $V_k = \mathrm{OCV}(\mathrm{SOC}_k) - i_k(R_s + R_d)$.

2.2. Capacity estimation with state projection

Given the measured electrical signals (i.e., cell current and terminal voltage), we can estimate the SOC by using one of the existing approaches such as the extended/unscented Kalman filter [1–3,8] and the coulomb counting technique [6]. In what follows, we intend to elaborate on the proposed capacity estimation method which utilizes the SOC estimates before and after the state projection to estimate the capacity. Based on a capacity estimate C_k, the state projection scheme projects the SOC through a time span $L\Delta t$, expressed as [8]

$$\mathrm{SOC}_{k+L} = \mathrm{SOC}_k + \frac{\int_{t_k}^{t_{k+L}} i(t)dt}{C_k} \tag{3}$$

The effect of the capacity on the projected SOC is graphically explained in Fig. 2, where the projected SOCs with larger/smaller-than-true capacity estimates exhibit positive/negative deviations from their true values under a constant current discharge. This observation has two implications: (1) the capacity significantly affects the SOC estimation and inaccurate capacity estimation leads to inaccurate SOC estimation; and (2) the SOCs before and after the state projection, if accurately estimated based on the voltage and current measurements, can be used along with the net charge flow to back estimate the capacity. The second implication can be mathematically expressed as

$$C_k = \frac{\int_{t_k}^{t_{k+L}} i(t)dt}{\mathrm{SOC}_{k+L} - \mathrm{SOC}_k} \tag{4}$$

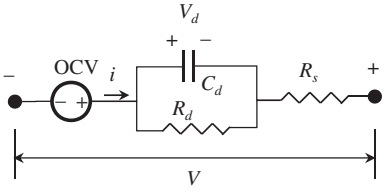

Fig. 1. Li-ion battery equivalent circuit model (or lumped parameter model): open circuit voltage (OCV), series resistance (R_i), diffusion resistance (R_d), and diffusion capacitance (C_d).

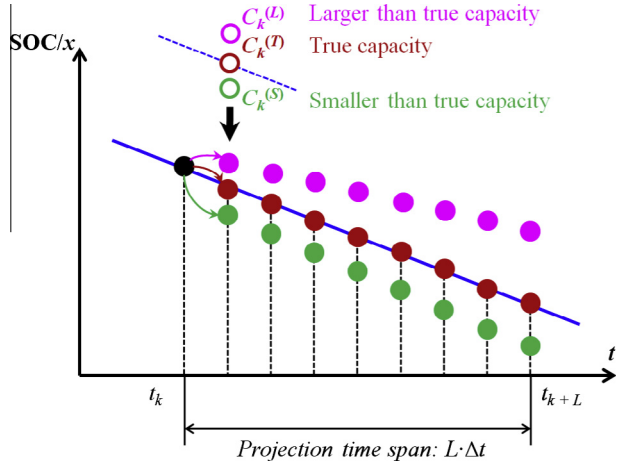

Fig. 2. Effect of capacity on state projection (assume a constant current discharge).

At the start of every state projection (i.e., at the time t_k), we need to have an accurate SOC estimate. This estimate will then be projected through the projection time span $L\Delta t$ according to the state projection equation in Eq. (4). Upon the completion of every state projection (i.e., at the time t_{k+L}), we also need to have an accurate SOC estimate to complete the capacity estimation. It is important to note that the accuracy in the SOC estimation is a key factor that affects the accuracy in the capacity estimation. In applications where the SOC estimates contain large measurement or estimation noise, the state projection expressed by Eq. (4) will result in inaccurate and biased capacity estimates, as also noted in [15]. In order to maintain good accuracy in the capacity estimation in the presence of inaccurate SOC estimates, we should ensure a large cumulated charge (i.e., the nominator in Eq. (4)) to compensate for the inaccuracy in the SOC estimation.

2.3. RUL prediction with Gauss–Hermite particle filter

2.3.1. Particle filter

To make the discussion more concrete, let us consider a dynamic nonlinear discrete-time system described by a state-space model. We define the nonlinear state-space model considered in this work as

$$\begin{aligned} \text{Transition}: &\quad \mathbf{x}_i = f(\mathbf{x}_{i-1}, \boldsymbol{\theta}_{i-1}) + \mathbf{u}_i, \boldsymbol{\theta}_i = \boldsymbol{\theta}_{i-1} + \mathbf{r}_i, \\ \text{Measurement}: &\quad \mathbf{y}_i = g(\mathbf{x}_i, \boldsymbol{\theta}_i) + \mathbf{v}_i \end{aligned} \tag{5}$$

where $\mathbf{x}_i$ is the vector of system states at the time $t_i = i\,\Delta t$, with Δt being a fixed time step between two adjacent measurement points, and i being the index of the measurement time step, respectively; $\boldsymbol{\theta}_i$ is the vector of system model parameters at the time t_i; $\mathbf{y}_i$ is the vector of system observations (or measurements); $\mathbf{u}_i$ and $\mathbf{r}_i$ are the vectors of process noise for states and model parameters, respectively; $\mathbf{v}_i$ is the vector of measurement noise; $f(\bullet,\bullet)$ and $g(\bullet,\bullet)$ are the state transition and measurement functions, respectively. With the system defined, we aim at inferring both the system states $\mathbf{x}$ and model parameters $\boldsymbol{\theta}$ from the noisy observations $\mathbf{y}$.

In a Bayesian framework, the posterior probability distribution functions (PDFs) of the states given the past observations, $p(\mathbf{x}_t|\mathbf{y}_{1:i})$, constitutes a statistical solution to the inference problem described in Eq. (5) and properly captures the uncertainties of the states. The recursive Bayesian filter enables a continuous update of the posterior PDFs with new observations. Particle filter, as a sequential Monte Carlo method, implements the recursive Bayesian filter by simulation-based methods. In the particle filter, the state posterior PDFs are built based on a set of particles and their associated weights both of which are continuously updated as new observations arrive, expressed as

$$p(\mathbf{x}_i|\mathbf{y}_{1:i}) \approx \sum_{i=1}^{N_P} \mathbf{w}_i^j \delta(\mathbf{x}_i - \mathbf{x}_i^j) \tag{6}$$

where $\{\mathbf{x}_i^j\}_{j=1}^{N_P}$ and $\{\mathbf{w}_i^j\}_{j=1}^{N_P}$ are the particles and weights estimated at the ith measurement time step, respectively; N_P the number of particles; and δ the Dirac delta function. The standard particle filter algorithm follows a standard procedure of sequential importance sampling and resampling (SISR) to recursively update the particles and their associated weights [16]:

(1) Initialization ($i = 0$)

For $j = 1,2,\ldots,N_P$, randomly draw state samples $\mathbf{x}_0^j$ from the prior distribution $p(\mathbf{x}_0)$.

(2) For $i = 1,2,\ldots$

(a) Importance Sampling

For $j = 1,2,\ldots,N_P$, randomly draw samples from the proposal importance density $\mathbf{x}_i^j \sim q(\mathbf{x}_i|\mathbf{x}_{0:i-1}^j, \mathbf{y}_{1:i})$. The standard SISR particle filter employs the so-called transmission prior distribution $q(\mathbf{x}_i|\mathbf{x}_{0:i-1}^j, \mathbf{y}_{1:i}) = p(\mathbf{x}_i|\mathbf{x}_{i-1}^j)$. For $j = 1,2,\ldots,N_P$, evaluate the importance weights

$$w_i^j = w_{i-1}^j \frac{p(\mathbf{y}_i|\mathbf{x}_i^j)p(\mathbf{x}_i^j|\mathbf{x}_{i-1}^j)}{q(\mathbf{x}_i|\mathbf{x}_{0:i-1}^j, \mathbf{y}_{1:i})} \tag{7}$$

For $j = 1,2,\ldots,N_P$, normalize the importance weights

$$\tilde{w}_i^j = w_i^j \left[\sum_{j=1}^{N_P} w_i^j\right]^{-1} \tag{8}$$

(b) Selection (Resampling)

Multiply/suppress samples $\{\mathbf{x}_i^j\}_{j=1}^{N_P}$ with respect to high/low importance weights to obtain N_P random samples $\{\mathbf{x}_i^j\}_{j=1}^{N_P}$ with equal weights N_P^{-1}.

(c) Posterior PDF Approximation with Eq. (6).

2.3.2. Gauss–Hermite particle filter

It is noted that the performance of the particle filter largely depends on the choice of the proposal importance density. The optimal proposal importance density is $q(\mathbf{x}_i|\mathbf{x}_{0:i-1}, \mathbf{y}_{1:i}) = p(\mathbf{x}_i|\mathbf{x}_{i-1}, \mathbf{y}_i)$ which utilizes the information carried by both the most recent state estimates $\mathbf{x}_{i-1}$ and system observations $\mathbf{y}_i$. The proposal density used in the standard SISR particle filter does not exploit the latest system observations $\mathbf{y}_i$ and, when the observations contain outliers (i.e., the observations are not informative) or, on the contrary, when the observations have a small noise variance (i.e., the observations are very informative), the standard SISR filter often produces poor performance [17]. One principle means to better approximate the optimal proposal density is local linearization using standard nonlinear filter methodologies to generate the proposal density. Research efforts in pursuit of a better proposal density resulted in the development of the Gauss–Hermite particle filter (GHPF) [18] which uses the Gauss–Hermite Kalman filter (GHKF) [19] to generate the proposal density. The GHPF is based on the so-called "Gauss–Hermite quadrature integration" and does not require the evaluation of the Jacobian matrix, which makes this filter technique computationally attractive as compared to the extended Kalman filter. The main idea of the GHPF is to propagate sufficient statistics for each particle based on the latest system observations, in order to build a more representative proposal density. The proposal density generated by running the GHKF allows the movement of the particles in the prior distribution to the regions of high likelihood. The GHKF algorithm of

the degree p is briefly presented below, which combines the particle filter and the GHKF:

(1) Initialization ($i = 0$)

For $j = 1,2,\ldots,N_P$, randomly draw state samples $\mathbf{x}_0^j$ from the prior distribution $p(\mathbf{x}_0)$.

(2) For $i = 1,2,\ldots$

(a) Importance Sampling

For $j = 1,2,\ldots,N_P$, randomly draw samples from a Gaussian proposal importance density $\mathbf{x}_i^j \sim q(\mathbf{x}_i|\mathbf{x}_{0:i-1}^j, \mathbf{y}_{1:i}) = \mathcal{N}(\mathbf{x}_i; \mu_{i|i}^j, \Sigma_{i|i}^j)$ generated by the GHKF [19].

(i) Generate $2p + 1$ Gauss–Hermite cubature points.

(ii) Predict the first- and second-order statistics of the state based on the cubature points with the state transmission equation (time update).

(iii) Update the first- and second-order statistics of the state based on the observation with the measurement function (measurement update).

For $j = 1,2,\ldots,N_P$, evaluate the importance weights using Eq. (7).

For $j = 1,2,\ldots,N_P$, normalize the importance weights Eq. (8).

(b) Selection (Resampling)

Multiply/suppress samples $\{\mathbf{x}_i^j\}_{j=1}^{N_P}$ with respect to high/low importance weights to obtain N_P random samples $\{\mathbf{x}_i^j\}_{j=1}^{N_P}$ with equal weights N_P^{-1}.

(c) Posterior PDF Approximation with Eq. (6).

2.3.3. Application of GHPF to RUL prediction

In this section, we apply the GHPF to predicting the RUL of Li-ion battery. The underlying capacity fade model can be expressed as an exponential function

$$c_i = \frac{C_i}{C_0} = 1 - \alpha[1 - \exp(-\lambda i)] - \beta i \tag{9}$$

where C_i is the capacity at the ith cycle, C_0 the initial capacity, α the coefficient of the exponential component of capacity fade, λ the exponential capacity fade rate, β the coefficient of the linear component of capacity fade, and c_i the normalized capacity at the ith cycle. It was reported that the exponential function captures the active material loss [20] and the hybrid of linear and exponential functions was reported to provide a good fit to three years' cycling data [21]. Here we treat the normalized capacity, c, as the state variable and the capacity fade rates, α, λ, and β as the model parameters. The system transition and measurement functions can then be written as

$$\begin{aligned} &\text{Transition}: && c_i = 1 - \alpha_{i-1}[1 - \exp(-\lambda_{i-1} i)] - \beta_{i-1} i + u_i, \\ & && \alpha_i = \alpha_{i-1} + r_{1,i}, \lambda_i = \lambda_{i-1} + r_{2,i}, \beta_i = \beta_{i-1} + r_{3,i} \\ &\text{Measurement}: && y_i = c_i + v_i \end{aligned} \tag{10}$$

Here, y_i is the capacity measurement (or the capacity estimate based on the state projection described in Section 2.2) at the ith cycle, u, r_1, r_2, r_3 and v are the Gaussian noise variables with zero means.

At the ith cycle, the posterior PDF of the normalized capacity is approximated by the GHPF as

$$p(c_i|y_{1:i}) \approx \frac{1}{N_P}\sum_{i=1}^{N_P}\delta(c_i - c_i^j) \tag{11}$$

where c_i^j is the jth particle after the resampling step at the ith cycle. The prediction of the normalized capacity forward by l cycles can be expressed as

$$p(c_{i+l}|y_{1:i}) \approx \frac{1}{N_P}\sum_{i=1}^{N_P}\delta(c_{i+l} - c_{i+l}^j) \tag{12}$$

where

$$c_{i+l}^j = 1 - \alpha_i^j[1 - \exp(-\lambda_i^j(i+l))] - \beta_i^j(i+l) \tag{13}$$

Here we define the normalized capacity being 78.5% as the failure threshold. Then the RUL (in cycles) can be obtained for each particle as the number of cycles between the current cycle i and the end-of-service (EOS) cycle

$$L_i^j = \text{root}[\alpha_i^j[1 - \exp(-\lambda_i^j i)] + \beta_i^j i = 0.215] - i \tag{14}$$

Finally, the RUL distribution can be build based on these particles, expressed as

$$p(L_i|y_{1:i}) \approx \frac{1}{N_P}\sum_{i=1}^{N_P}\delta(L_i - L_i^j) \tag{15}$$

This completes the derivation of the RUL distribution approximated by the GHPF. Overall speaking, the RUL prediction employs the GHPF technique to adaptively adjust an underlying capacity fade model with new capacity estimates from the state projection scheme described in Section 2.2 and projects the capacity to the EOS value with the latest fade model in order to determine the RUL.

2.4. Overall procedure

The overall procedure of the integrated method for the capacity estimation and RUL prediction is illustrated in Fig. 3. This method essentially consists of two modules: the capacity estimation module (detailed in Section 2.2) and the RUL prediction module (detailed in Section 2.3). Starting with the first cycle, the method first implements the capacity estimation module where the SOC

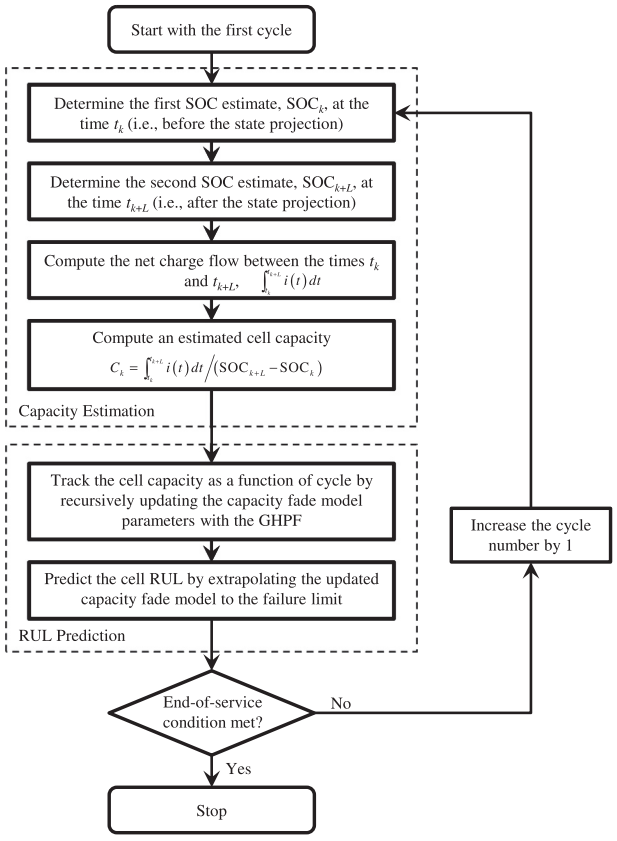

Fig. 3. A flowchart of the proposed integrated method for the capacity estimation and RUL prediction of Li-ion battery.

estimates before and after the state projection are used along with the net charge flow to estimate the cell capacity. After the capacity estimate is obtained, the RUL prediction module is then implemented to track the cell full capacity as a function of cycle by recursively updating the capacity fade model parameters and to predict the cell's EOS cycle by extrapolating the updated capacity fade model to the failure limit. This process is iteratively executed every cycle until the EOS condition is met (or the failure limit is reached).

3. Experimental results

The verification of the proposed method was accomplished by conducting 10 years' continuous cycling test on four test cells in the lab as well as post-explant cycling test on four field cells with 4–7 implant years. This section reports the results of these tests. Section 3.1 presents the test procedure along with the cycling performance of the test cells. The capacity estimation and RUL prediction results are reported in Sections 3.2 and 3.3, respectively.

3.1. Test procedure and cycling data

Li-ion cells were constructed in hermetically sealed prismatic cases between 2002 and 2012 and subjected to full depth of discharge cycling with a nominally weekly discharge rate ($C/150$ discharge) under 37 °C. The weekly rate discharge capacities are plotted against the time on test in Fig. 4. Please note that, for confidentiality reasons, the discharge capacity of a cell in Fig. 4 and in the discussions thereafter is presented after being normalized by the beginning-of-life (BOL) discharge capacity of the cell. The cycling data from four 2002 cells will be used to verify the effectiveness of the proposed method in the capacity estimation and RUL prediction. As shown in Fig. 4, 80% of the initial capacity is retained even after 10 years of repeated cycling at an elevated temperature, indicating exceedingly stable cell performance. The cycling data also indicate consistent performance of cells manufactured over a large time period.

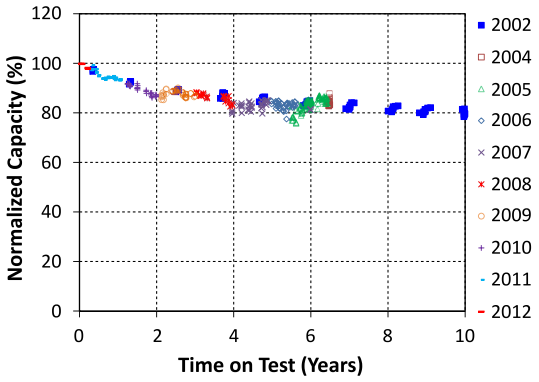

Fig. 4. Cycling performance of cells manufactured and cycled between 2002 and 2012.

The voltage curve evolution from one test cell is graphically plotted against the normalized discharge capacity (relative to the BOL discharge capacity) and the depth of discharge (DOD or 1 − SOC) in Fig. 5(a) and (b), respectively. It can be observed from

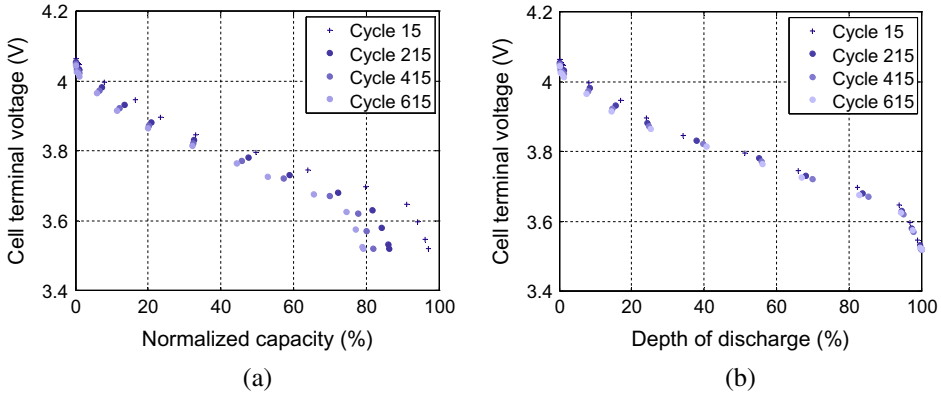

Fig. 5. Voltage curve evolution in weekly cycling test. Figure (a) plots the voltage versus normalized discharge capacity curves at cycles 15 (0.3 years on test), 215 (3.5 years), 415 (6.5 years) and 615 (9.3 years) and (b) plots the voltage versus DOD curves at these four cycles.

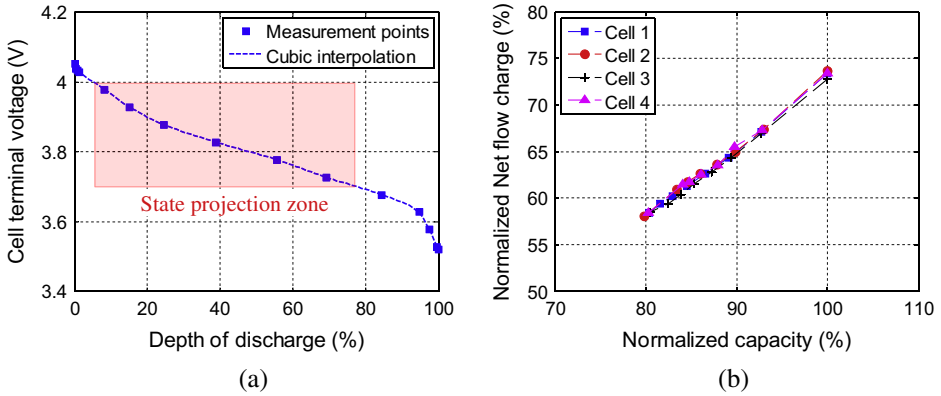

Fig. 6. Plot of OCV as a function of DOD with state projection zone (a) and plot of normalized net charge flow as a function of normalized discharge capacity (b).

Fig. 5(a) that the voltage versus discharge capacity curves shrink to the left due to the capacity fade over time. In contrast, the voltage versus DOD curve in Fig. 5(b) exhibited very minor evolutions in the first 2 years and minimal evolutions thereafter. Lack of any significant changes in the shape of the curve is indicative of stability of the individual electrodes, active materials, electrode impedances, and so forth. It is noted that, after a certain time delay (greater than 5τ), the diffusion RC circuit in Fig. 1 becomes simply a resistor and that, under the extremely low discharge rate ($C/168$), the IR effect is very minimal, i.e., $i_k(R_s + R_d) \approx 0$. Under these two conditions, the cell terminal voltage closely resembles the cell OCV. Thus, the observation from Fig. 5(b) can be stated as "the relationship between the OCV and DOD remains almost unchanged in the presence of cell aging". This observation supports the use of the OCV–DOD or OCV–SOC relationship for the capacity estimation.

3.2. Capacity estimation results

3.2.1. Test cells

The cell discharge capacity is estimated based on the state projection scheme described in Section 2.2. In this study, an unknown SOC (or 1 − DOD) at a specific OCV level is approximated based on the cubic spline interpolation with a set of known OCV and SOC values (see the measurement points and interpolated curve in Fig. 6(a)). As shown in Fig. 6(a), the state projection zone spans an OCV range 4.0–3.7 V. It is noted that, in addition to the state projection zone shown in Fig. 6(a) that is used in this study, the state projection scheme can also work with other state projection zones that do not span an OCV range 4.0–3.7 V. In Fig. 6(b), the net charge flow in this state projection zone is plotted as a function of cell discharge capacity for four test cells (cells 1–4) at eight different cycles spanning the whole 10 years' test duration. The graph shows that the net charge flow is a linear function of the cell discharge capacity. This observation suggests that a linear model can be generated to relate the capacity to the current integration. In fact, this linear model is exactly the one given in Eq. (4). With the SOCs at 4.0 V and 3.7 V derived based on the OCV–SOC relationship and the net charge flow calculated by the coulomb counting, the cell discharge capacity can be computed based on Eq. (4).

The capacity estimation results for the four cells are shown in Fig. 7. It can be observed that the capacity estimation method closely tracks the capacity fade trend throughout the cycling test for all the four cells. Table 1 summarized the capacity estimation errors for the four cells. Here, the root mean square (RMS) and maximum errors are formulated as

$$\varepsilon_{RMS} = \sqrt{\frac{1}{N_C}\sum_{i=1}^{N_C}(\Delta\hat{C}_i - \Delta C_i)^2}, \quad \varepsilon_{Max} = \max_{1\leqslant i\leqslant N_C}|\Delta\hat{C}_i - \Delta C_i| \tag{16}$$

Table 1
Capacity estimation results of 4 test cells.

Cell	Cell 1	Cell 2	Cell 3	Cell 4
RMS error (%)	0.52	0.51	0.88	0.52
Maximum error (%)	2.38	2.91	2.10	2.90

Table 2
Capacity estimation results of 4 field cells.

Cell	Cell 5	Cell 6	Cell 7	Cell 8
Implant years	6.87	6.23	5.43	4.31
Measured capacity (%)	84.92	87.33	86.91	87.96
Estimated capacity (%)	85.56	86.72	87.05	88.66
Estimation error (%)	0.64	0.61	0.14	0.70

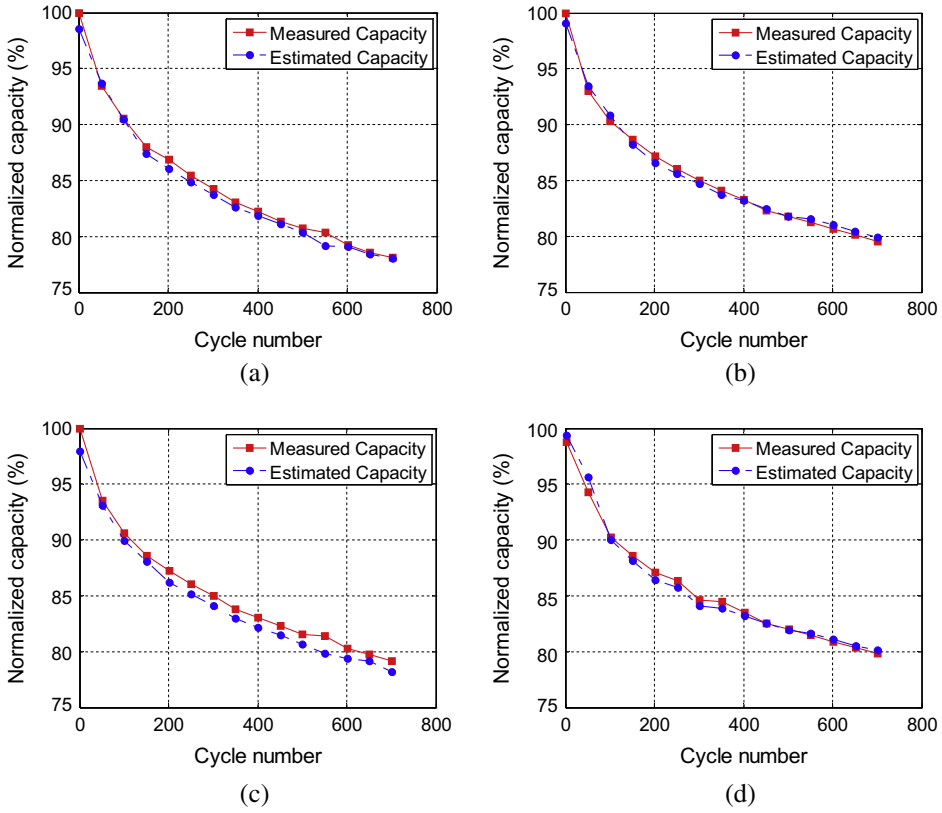

Fig. 7. Capacity estimation results of cell 1 (a), cell 2 (b), cell 3 (c) and cell 4 (d). Results are plotted every 50 cycles for the ease of visualization.

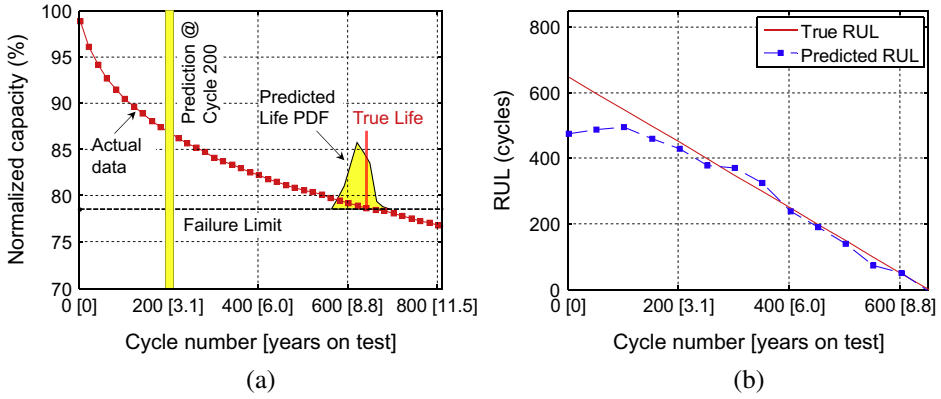

Fig. 8. RUL prediction results of cell 1. Figure (a) plots the capacity tracking and RUL prediction by the GHPF at cycle 200 (results are plotted every 20 cycles for the ease of visualization) and (b) plots the RUL predictions by the GHPF at multiple cycles throughout the life-time.

where N_C is the number of charge/discharge cycles; and ΔC_i and $\Delta \hat{C}_i$ are respectively the measured and estimated normalized capacities at the ith cycle. It can be observed that the average error is less than 1% for any of the four cells and the maximum error is less than 3%. The results suggest that the state projection method is capable of producing accurate and robust capacity estimation in the presence of cell-to-cell manufacturing variability. The good accuracy in the capacity estimation results from accurate SOC estimation that can be attributed to two facts: (i) under the extremely low discharge rate (C/168), the cell terminal voltage closely resembles the cell OCV, which ensures good accuracy in the cell OCV; and (ii) the OCV–SOC relationship remains almost unchanged over repeated cycling, which, along with the accurate OCV values, leads to accurate SOC estimation.

3.2.2. Field cells

Four Li-ion prismatic cells were obtained from the devices after 4–7 implant years. The four field cells then underwent full depth of discharge cycling with a nominally weekly discharge rate (C/168 discharge) under 37 °C. The full DOD weekly cycling data were used to estimate the discharge capacities of the cells based on the state projection scheme described in Section 2.2. The capacity estimation results of these four cells are summarized in Table 2. Both the measured and estimated discharge capacities presented in Table 2 are normalized by the estimated BOL discharge capacity. It can be observe that the errors are below 1% for all the four field cells. The capacity estimate results on real field cells further verify that the proposed state projection scheme is considerably effective for the capacity estimation of Li-ion battery.

3.3. RUL prediction results

The RUL is used as the relevant metric for determining the state of life (SOL) of Li-ion battery. Based on the capacity estimates obtained with the state projection scheme, the GHPF technique is used to project the capacity fade trend to the EOS value (or the failure limit) for the RUL prediction. Here the failure limit is defined as 78.5% of the BOL discharge capacity. Fig. 8(a) shows the capacity tracking and RUL prediction by the GHPF at cycle 200 (or 3.1 years). It can be observed that the predicted PDF of the life provides a slightly conservative solution and includes the true EOS cycle (i.e., 650 cycles or approximately 9.4 years). Fig. 8(b) plots the RUL predictions by the GHPF at multiple cycles throughout the life-time. The graph shows that, as we keep updating the RUL distribution throughout the battery life-time, the prediction tends to converge to the true value as the battery approaches its EOS cycle.

4. Conclusion

This paper presents an integrated method for the capacity estimation and RUL prediction of Li-ion battery under actual use condition, which allows for early and proactive identification and resolution of reliability issues as well as supports optimal decision-making on maintenance. This method provides users of Li-ion battery-powered implantable medical devices with estimates of both the capacity (spanning a single discharge cycle) and the RUL (spanning the whole service life). The capacity estimate enables the prediction of remaining useful time that informs the users about how long the battery can still be used before the next recharge. Since the capacity is updated every cycle to account for the aging effects, the method is expected to produce an accurate estimate of remaining useful time. The RUL allows the users to schedule an optimal replacement near the EOS so that the devices can be used as long as possible and, at the same time, users' safety is not compromised. Our contributions to the battery prognostics are the derivation of a state-projection scheme for the capacity estimation based on the author's previous study [8] and the use of the Gauss–Hermite particle filter technique for the RUL prediction. Experiments with 10 years' continuous cycling data and post-explant cycling data verify that the proposed method achieves accurate capacity estimation and suggest that the proposed method is a promising methodology for the battery prognostics. Future work will investigate the effect of the dynamic loading condition on the accuracy in the capacity estimation as well as extend the proposed method to the impedance estimation.

References

[1] Plett GL. Extended Kalman filtering for battery management systems of LiPB-based HEV battery packs Part 3. State and parameter estimation. J Power Sources 2004;134(n2):277–92.
[2] Plett GL. Sigma-point Kalman filtering for battery management systems of LiPB-based HEV battery packs Part 2: Simultaneous state and parameter estimation. J Power Sources 2006;161(n2):1369–84.
[3] Lee S, Kim J, Lee J, Cho BH. State-of-charge and capacity estimation of lithium-ion battery using a new open-circuit voltage versus state-of-charge. J Power Sources 2008;185(n2):1367–73.
[4] Zhang Q, White RE. Capacity fade analysis of a lithium ion cell. J Power Sources 2008;179(n2):793–8.
[5] Zhang Q, White RE. Calendar life study of Li-ion pouch cells Part 2: Simulation. J Power Sources 2008;179(n2):785–92.
[6] Ng KS, Moo CS, Chen YP, Hsieh YC. Enhanced coulomb counting method for estimating state-of-charge and state-of-health of lithium-ion batteries. Appl Energy 2009;86(n9):1506–11.
[7] Sun YH, Jou HL, Wu JC. Auxiliary health diagnosis method for lead-acid battery. Appl Energy 2010;87(n9):3691–8.
[8] Hu C, Youn BD, Chung J. A multiscale framework with extended Kalman filter for lithium-ion battery SOC and capacity estimation. Appl Energy 2012;92:694–704.

[9] Waag W, Sauer DU. Adaptive estimation of the electromotive force of the lithium-ion battery after current interruption for an accurate state-of-charge and capacity determination. Appl Energy 2013;111:416–27.
[10] Xiong R, Sun F, Chen Z, He H. A data-driven multi-scale extended Kalman filtering based parameter and state estimation approach of lithium-ion polymer battery in electric vehicles. Appl Energy 2014;113:463–76.
[11] Saha B, Goebel K, Poll S, Christophersen J. Prognostics methods for battery health monitoring using a Bayesian framework. IEEE Trans Instr Meas 2009;58(n2):291–6.
[12] Saha B, Goebel K. Modeling Li-ion battery capacity depletion in a particle filtering framework. In: Proceedings of annual conference of the PHM society. San Diego, CA; September 27–October 1.
[13] Liu J, Saxena A, Goebel K, Saha B, Wang W. An adaptive recurrent neural network for remaining useful life prediction of lithium-ion batteries. In: Annual conference of the prognostics and health management society. Portland, Oregon; October 2010.
[14] Ng SSY, Xing Y, Tsui KL. A naive Bayes model for robust remaining useful life prediction of lithium-ion battery. Appl Energy 2014;118:114–23.
[15] Plett G. Recursive approximate weighted total least squares estimation of battery cell total capacity. J Power Sources 2011;196(n4):2319–31.
[16] Arulampalam S, Maskell S, Gordon N, Clapp T. A tutorial on particle filters for on-line non-linear/non-Gaussian Bayesian tracking. IEEE Trans Signal Process 2002;50(n2):174–88.
[17] Cappe O, Godsill SJ, Moulines E. An overview of existing methods and recent advances in sequential monte carlo. IEEE Proc 2007;95(n5):899–924.
[18] Yuan Z, Zheng N, Jia X. The Gauss–Hermite particle filter. Acta Electr Sinica 2003;31(n7):970–3.
[19] Ito K, Xiong K. Gaussian filters for nonlinear filtering problems. IEEE Trans Automatic Control 2000;45:910–27.
[20] Honkura Kohei, Takahashi Ko, Horiba Tatsuo. Capacity-fading prediction of lithium-ion batteries based on discharge curves analysis. J Power Sources 2011;196(n23):10141–7.
[21] Brown Jason, Scott Erik, Schmidt Craig, Howard William. A practical longevity model for lithium-ion batteries: de-coupling the time and cycle-dependence of capacity fade. In: 208th ECS Meeting; 2006, Abstract #239.